NANO REVIEWS
Organizing Nanoscience and Nanotechnology for the Future

COACTION PUBLISHING

NANOSTRUC 2014

Highly textured and transparent RF sputtered Eu_2O_3 doped ZnO films

Remadevi Sreeja Sreedharan[1], Vedachalaiyer Ganesan[2], Chellappan Pillai Sudarsanakumar[3], Kaushalkumar Bhavsar[4], Radhakrishna Prabhu[4] and Vellara Pappukutty Pillai Mahadevan Pillai[1]*

[1]Department of Optoelectronics, University of Kerala, Thiruvananthapuram, India; [2]UGC-DAE Consortium for Scientific Research, Indore, India; [3]School of Pure and Applied Science, Mahatma Gandhi University, Kottayam, India; [4]School of Engineering, Robert Gordon University, Aberdeen, UK

Received: 27 November 2014; Revised: 9 December 2014; Accepted: 5 January 2015; Published: 11 March 2015

Background: Zinc oxide (ZnO) is a wide, direct band gap II-VI oxide semiconductor. ZnO has large exciton binding energy at room temperature, and it is a good host material for obtaining visible and infrared emission of various rare-earth ions.
Methods: Europium oxide (Eu_2O_3) doped ZnO films are prepared on quartz substrate using radio frequency (RF) magnetron sputtering with doping concentrations 0, 0.5, 1, 3 and 5 wt%. The films are annealed in air at a temperature of 773 K for 2 hours. The annealed films are characterized using X-ray diffraction (XRD), micro-Raman spectroscopy, atomic force microscopy, ultraviolet (UV)-visible spectroscopy and photoluminescence (PL) spectroscopy.
Results: XRD patterns show that the films are highly c-axis oriented exhibiting hexagonalwurtzite structure of ZnO. Particle size calculations using Debye-Scherrer formula show that average crystalline size is in the range 15–22 nm showing the nanostructured nature of the films. The observation of low- and high-frequency E_2 modes in the Raman spectra supports the hexagonal wurtzite structure of ZnO in the films. The surface morphology of the Eu_2O_3 doped films presents dense distribution of grains. The films show good transparency in the visible region. The band gaps of the films are evaluated using Tauc plot model. Optical constants such as refractive index, dielectric constant, loss factor, and so on are calculated using the transmittance data. The PL spectra show both UV and visible emissions.
Conclusion: Highly textured, transparent, luminescent Eu_2O_3 doped ZnO films have been synthesized using RF magnetron sputtering. The good optical and structural properties and intense luminescence in the ultraviolet and visible regions from the films suggest their suitability for optoelectronic applications.

Keywords: *visible photoluminescence*; *dielectric constants*; *micro-Raman spectra*; *optical constants*; *residual stress*

Responsible Editor: Dr Raquel Verdejo, Instituto de Ciencia y Tecnología de Polímeros, CSIC, Madrid, Spain.

Zinc oxide (ZnO) is a II-VI oxide semiconductor with wide, direct band gap energy of 3.37 eV at room temperature; hence, it is highly transparent in the visible region with a sharp cut-off around 380 nm (1, 2). It is widely used for transparent conducting electrodes, window material, flat panel displays, and so on (3). The band structure and optical properties of ZnO are similar to GaN, which is commonly used for the fabrication of photonic devices in the UV range. ZnO has a large excitonic binding energy of 60 meV at room temperature which is larger than that of GaN (25 meV), making it suitable for exciton related applications due to the extreme stability of excitons (4, 5). ZnO has high mechanical, thermal, and chemical stabilities and radiation hardness (6). Due to these attractive features, ZnO nanostructures gains significant attention for the fabrication of low-voltage and short-wavelength optoelectronic devices such as blue and ultraviolet light emitters, laser diodes, phosphorescent displays, photo detectors, transparent ultra violet protection films, gas sensors, and so on (7–10).

Several deposition techniques such as pulsed laser deposition (PLD), molecular beam epitaxy (MBE), spin coating, chemical vapor deposition (CVD), spray pyrolysis, sputtering, and so on are employed for the preparation of high-quality ZnO thin films (11–16). In continuation of our earlier works on the zinc oxide nanostructured films

Citation: Nano Reviews 2015, **6:** 26759 - http://dx.doi.org/10.3402/nano.v6.26759

(17–20), Eu_2O_3 doped ZnO films are prepared using RF magnetron sputtering for various doping concentrations to study the effect of dopants on the structural, morphological, optical, and luminescence properties of the ZnO nanostructures.

Experiment

Eu_2O_3 doped ZnO films are deposited on cleaned quartz substrate at room temperature (300 K) using radio frequency (RF) magnetron sputtering technique (RF frequency: 13.56 MHz). Pressed ZnO powder (Aldrich 99.99%) with various europium oxide concentrations is used as the target for sputtering. The Eu_2O_3 doping concentrations used for preparing the films are 0, 0.5, 1, 3, and 5 wt%. The sputter chamber is initially evacuated to a base pressure of 5×10^{-6} mbar. Argon gas is admitted into the chamber, and argon pressure is maintained at 0.02 mbar. The target is powered through a magnetron power supply (Advanced Energy MDX 500, Colorado). The sputtering is carried out under constant RF power of 150 watts for 30 min. The distance between target and substrate is maintained at 5×10^{-2} m.The deposited films are annealed in air at 773 K for 2 hours. The annealed films with Eu_2O_3 doping concentrations 0, 0.5, 1, 3, and 5 wt% are designated as E0, E0.5, E1, E3, and E5, respectively.

The structural, morphological optical and luminescent properties of the annealed films are investigated in detail. The crystalline quality and crystallographic orientation of the films are investigated using X-ray diffraction analysis (Brucker D8 Advance X-ray diffractometer, Germany) using Cu Kα1 radiation of wavelength 1.5406 A° in the 2θ range 20–70°. The vibrational spectra of the films are recorded using micro-Raman spectrometer (Labram HR-800, Horiba JobinYvon, Germany) using a laser radiation of wavelength 514.5 nm from an argon ion laser. The spectra are recorded with a spectral resolution of 1 cm^{-1}. The surface morphology of the films is investigated using atomic force microscopy (AFM) (Digital Instruments Nanoscope III, USA) analysis. The FESEM measurements are carried out using Nova Nano SEM–450 (Model No.1027647, FEI, USA) equipped with XFlash detector 6/10 (Bruker) and elemental analysis of the films are carried out using electron energy dispersive X-ray spectrometer (EDS-Quantax 200, Germany). The transmittance and reflectance spectra of the films in the spectral range 200–900 nm are recorded using JASCO V-550 (Japan) UV-visible double beam spectrometer. The thickness of the films is measured using Dektak stylus profilometer (USA) and also using vertical SEM measurements. Photoluminescence spectra of the samples are recorded using Perkin Elmer LS50B (USA) luminescence spectrometer.

Results and discussion

XRD analysis

The X-ray diffraction patterns of Eu_2O_3 doped ZnO films at different doping concentrations are shown in Fig. 1. The XRD patterns of all the films present a single sharp intense peak at 2θ value 34.9° corresponding to (002) plane of hexagonal wurtzite structure of ZnO (JCPDS card No-75-0576). Thus, the films present a single crystalline like structure with c-axis orientation. The c-axis orientation of the films is due to the lowest surface energy of (001) basal plane in ZnO and minimization of internal stress leading to preferred growth along [001] direction (21, 22). Even after europium doping, the wurtzite crystal structure is preserved in all the films. Also, no spurious phase such as europium oxide is observed within the detection limit. All these show that Eu_2O_3 is well dissolved in the ZnO lattice.

The d-value of the films is calculated using Bragg's relation (23).

$$n\lambda = 2d_{hkl} \sin \theta_{hkl} \quad (1)$$

where λ is the wavelength of the X-ray radiation and θ_{hkl} is the angle of diffraction. The calculated values of the inter-planar distance 'd_{hkl}' for the films is given in Table 1.

It can be seen that the intensity of (002) peak in moderately doped films (E0.5, E1, and E3) is slightly greater than that of the undoped film. But the intensity of this peak is the lowest in E5 film. Thus, it can be seen that the moderate doping of Eu_2O_3 enhances the crystallinity of the films. It is found that the FWHM of the (002) peak in the Eu_2O_3 doped films are greater than that of undoped film. This indicates that the doped films have more stress compared to the undoped film. The ionic radius of Zn^{2+} is 0.74 A° and that of Eu^{3+} is 0.947 A° (24). The mismatch in the ionic radii of the dopant and host cation can be the reason for enhanced FWHM of the doped films which can introduce stress in the films. The 2θ value of the Eu_2O_3 doped films is slightly lower than that of undoped film, which means an increase in d_{002} as expected from Bragg's law. This may be attributed to the bigger size of the Eu^{3+} ion compared to the Zn^{2+} ion. The substitution of Eu^{3+} ion into the ZnO lattice may result in the expansion of the lattice. The average size of the crystallites (D_{hkl}) in the films is estimated using the following Debye-Scherer' formula (23).

$$D_{hkl} = \frac{0.9\lambda}{\beta_{hkl} \cos \theta_{hkl}} \quad (2)$$

where λ is the wavelength of X-ray radiation (1.5406A°), θ_{hkl} is the Bragg diffraction angle, and β_{hkl} is the FWHM of the diffraction peak in radian. The undoped film shows an average crystalline size of 27 nm. The E0.5, E1, and E3 films show an average crystalline size of 16 nm.

Citation: Nano Reviews 2015, 6: 26759 - http://dx.doi.org/10.3402/nano.v6.26759

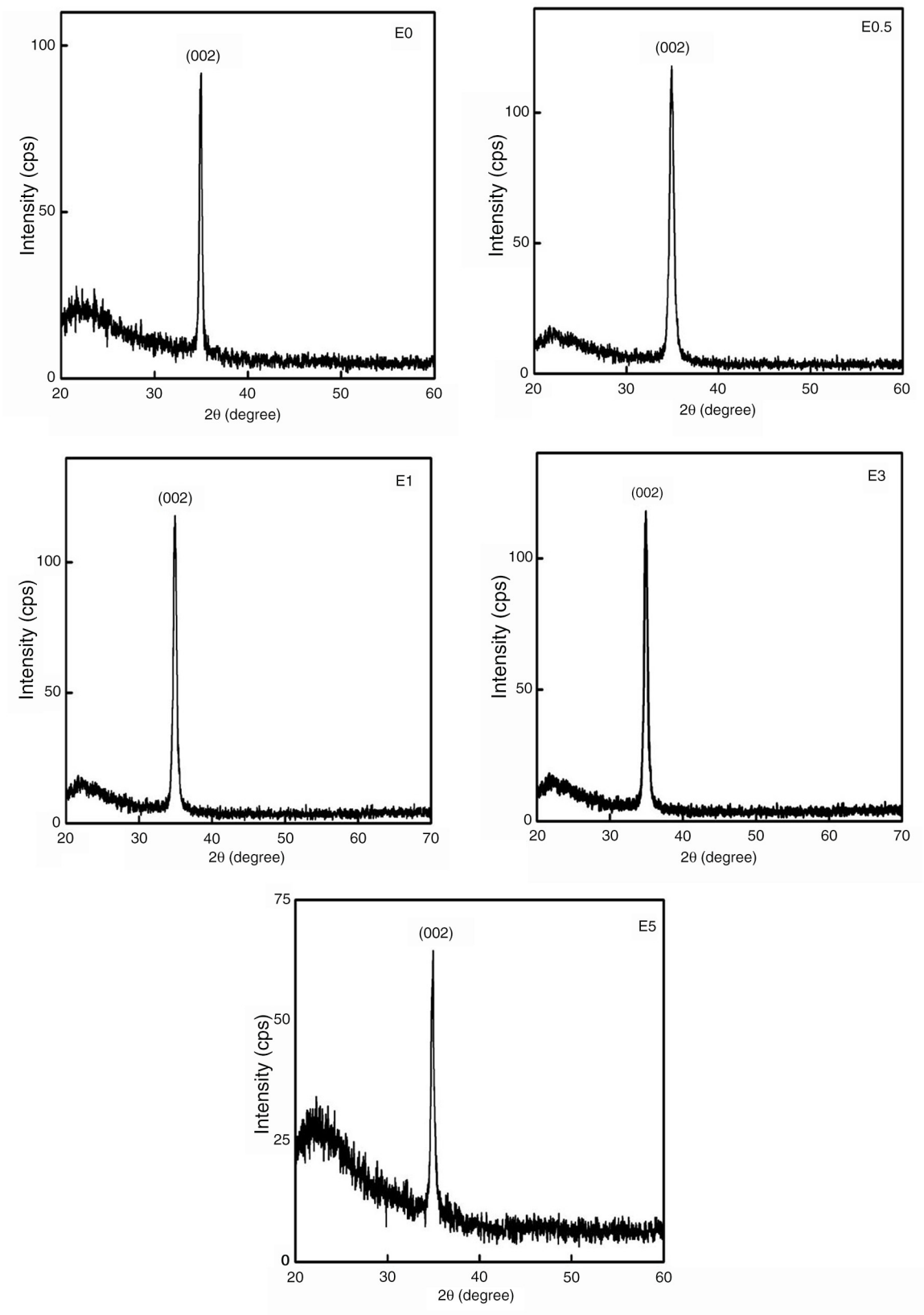

Fig. 1. X-ray diffraction patterns of RF sputtered Eu_2O_3 doped ZnO films (Eu_2O_3 doping concentrations – 0, 0.5, 1, 3, and 5 wt%) on quartz substrates and annealed at 773K.

Table 1. Structural parameters of RF sputtered pure and Eu_2O_3 dopedZnO films (Eu_2O_3 doping concentrations – 0, 0.5, 1, 3 and 5 wt%) on quartz substrates and annealed at 773K

Films	d_{hkl} (A°)	Crystallite size D_{hkl} (nm)	Lattice constant c (A°)	Strain	Stress (GPa)
E0	2.5728	26.8	5.1314	−0.0122	5.5357
E0.5	2.5753	15.9	5.1363	−0.0113	5.1117
E1	2.5753	15.9	5.1363	−0.0113	5.1117
E3	2.5753	16.9	5.1363	−0.0113	5.114
E5	2.5763	22.1	5.1384	−0.0109	4.9274

The E5 film shows an average crystalline size of 22 nm. Thus, all the films are nanostructured in nature.

According to the hexagonal symmetry the lattice constants can be evaluated using the following equation,

$$\frac{1}{d_{hkl}^2} = \frac{4}{3}\left(\frac{h^2 + hk + k^2}{a^2}\right) + \frac{l^2}{c^2} \tag{3}$$

where a and c are the lattice parameters h, k, and l are the miller indices of the plane and d_{hkl} is the inter-planar spacing. The lattice constant c of the films is calculated and is given in Table 1. It is observed that the lattice parameter c in the doped films is slightly larger than that of the undoped film. The increase in the lattice constant c in the doped films compared to the undoped film indicates slight expansion of the lattice due to the substitution of Eu^{3+} at Zn^{2+} sites. The introduction of dopant and the lattice mismatch between film and substrate can introduce strain in the films. This strain can affect the structure and properties of the film to some extent. The strain along the c-axis is calculated using the expression (25),

$$\varepsilon(\%) = \frac{c - c_0}{c_0} \times 100 \tag{4}$$

where ε is the strain along the c-axis perpendicular to the substrate surface. Combined with the elastic constants of single crystalline ZnO, the stress in the films can be calculated using the biaxial strain model (26),

$$\sigma = -453.6 \times \frac{c - c_0}{c_0}\, GPa \tag{5}$$

where c is the lattice constant of the film calculated from the XRD data and c_0 is the strain-free lattice constant obtained from the JCPDS data card. The positive value of stress indicates that the films are in a state of tensile stress. The biaxial tensile stress in the films is found to be decreasing from 5.54 to 4.93 GPa with Eu_2O_3 doping. The stress developed in the thin films is generally related to growth parameters, substrate on which the film is deposited, defects, impurities, and lattice distortion in the films (6, 27). The stress associated with defects and impurities are termed as intrinsic stress, while that originating from lattice mismatch and difference in thermal expansion coefficient (TEC) between film and substrate is termed as extrinsic stress (28). The stress originating from lattice mismatch between film and substrate in these films is difficult to calculate due to the amorphous nature of quartz substrate (28). It is generally assumed that the lattice mismatch strain is relieved at growth temperature by the formation of dislocations near the interface between film and substrate. However, the dislocation process freezes out on cooling and strain develops due to the difference in TECs of the film and substrate (29, 30). The stress introduced due to the difference in TECs of the film and substrate is given by the following equation,

$$\sigma_{th} = \int_{T_{growth/anneal}}^{RT} \left(\alpha^s - \alpha^b\right) \frac{E}{1 - \nu} dT \tag{6}$$

where α^s and α^b are the TEC of substrate and corresponding bulk material respectively. E is the Young's modulus and v is the Poisons ratio of the material. In the present study, the films are annealed in air at a temperature of 773K. TEC values for quartz substrate and ZnO are $\alpha^s = 0.59 \times 10^{-6}/K$ and $\alpha^b = 2.9 \times 10^{-6}/K$, respectively. The Young's modulus E and Poisson's ratio v of ZnO are 100 GPa and 0.36, respectively. Substituting these values in equation [6], the thermal stress of the ZnO film is calculated and is found to be $\sim$0.17 GPa. From equation [6], it is found that the thermal stress for the ZnO film deposited on quartz substrate increases with increasing annealing temperature. The undoped film shows a tensile stress of 5.54 GPa. This shows that the thermal stress is small in comparison with the observed stress in the films. Hence, the stress in the films is likely to be intrinsic in nature, contributed by the growth process rather than thermal origin (31). This indicates that the total stress in the film is highly influenced by the sputtering process and is mainly attributed to the implantation of particles sputtered from the oxide target into the growing film. Mohanty et al. reported that the surface oxygen is easily ionized during sputtering of the oxide target, and then gets accelerated with energy corresponding to full-potential drop across the cathode sheath. Even though these negative ions are neutralized during their transit, they reach the substrate with sufficient energy for implantation (28, 29). The bigger size of Eu^{3+} ion compared to Zn^{2+} ion results in the expansion of the lattice, which may produce deformation of the lattice and thereby introduce strain in the doped films.

Citation: Nano Reviews 2015, **6**: 26759 - http://dx.doi.org/10.3402/nano.v6.26759

Micro-Raman analysis

ZnO with hexagonal wurtzite structure has a space group c_{6v}^4 (p63mc) with two formula units per primitive cell. All zinc and oxygen atoms occupy c_{3v} site. Group theoretical analysis based on Fately et al. (32), yields nine optical modes (excluding the three acoustic modes) and are distributed as

$$\Gamma_{opt} = A_1 + 2B_1 + E_1 + 2E_2 \quad (7)$$

Of these, the A_1 and E_1 modes are both Raman and IR active, whereas E_2 modes are only Raman active and B_1 modes are inactive in both the spectra. The A_1 and E_1 modes are polar and splits into transverse optical (TO) and longitudinal optical (LO) modes. The E_2 mode is non-polar with two frequencies: E_2(High) and E_2(Low).

Figure 2 shows the micro-Raman spectrum of bulk ZnO powder. The Raman spectrum of ZnO powder presents two very intense bands at 100 and 437 cm^{-1}, medium intense band at 332 cm^{-1} and weak bands at 202, 379, 410, and 584 cm^{-1}.

Based on earlier works, the frequencies of fundamental optical modes in ZnO can be assigned as follows; $E_2(\text{Low}) = 100\,cm^{-1}$, $E_2(\text{High}) = 437\,cm^{-1}$, $A_1(TO) = 379\,cm^{-1}$, $E_1(TO) = 410\,cm^{-1}$, and $E_1(LO) = 584\,cm^{-1}$. The band observed at 202 cm^{-1} may be assigned to $2E_2$(Low) and the band at 332 cm^{-1} to $E_2(\text{High}) - E_2(\text{Low})$.

Figure 3 gives the micro-Raman spectra of undoped and Eu_2O_3 doped ZnO films. The low-frequency E_2 mode is observed $\sim$100 cm^{-1} in undoped and Eu_2O_3 doped ZnO films. The low-frequency mode is associated with the vibration of Zn sub-lattice (33–35). Raman spectra of both the pure and Eu_2O_3 doped ZnO films present an intense Raman band $\sim$438 cm^{-1} which can be attributed to E_2(High) mode. This mode is related to the vibration of oxygen atoms and is considered as the Raman fingerprint of wurtzite ZnO phase (36). The medium intense band $\sim$582 cm^{-1} in the Raman spectra of all the films can be due to $E_1(LO)$ mode which is associated with the formation of various crystal defects such as oxygen vacancy, zinc interstitials, and so on in the films (37). The $A_1(TO)$ mode and $E_1(TO)$ mode can be expected $\sim$380 and 407 cm^{-1} respectively (38). Raman spectrum of powder sample presents these modes as weak bands $\sim$379 and 410 cm^{-1}. But in the Raman spectra of the films these modes are not seen vividly. The $A_1(LO)$ mode is observed as a weak band $\sim$538 cm^{-1} in the Raman spectra of bulk ZnO (39). But in the Raman spectra of the films this mode is not observed. Many authors assigned the band $\sim$332 cm^{-1} as the difference mode $E_{2\text{high}}$–$E_{2\text{low}}$ (40).

Compared to the Raman spectrum of ZnO powder (bulk), the Raman spectra of films present a broad spectral feature. Here the ZnO is deposited on amorphous quartz substrate and the films have residual stress. The broad nature of Raman spectra of the films can be due to this residual stress. The measured thickness of the films is in the range 83–94 nm and hence the spectral contribution from the substrate can also be expected in the Raman spectra of the films. The medium intense band around 488 cm^{-1} can be due to the contribution from the quartz substrate. Compared to the Raman spectra of other films, the Raman spectrum of 5 wt% Eu_2O_3 doped film presents broader spectral feature. This can be attributed to the decline in crystallinity due to the higher doping concentration in this film as evident from the XRD analysis.

In the present study, the E_2(High) mode for the undoped film is observed at 438 cm^{-1}. The E_2(High) mode of the E 0.5 film also appears at 438 cm^{-1}, but it is broadened. For E1 and E3 films, the E_2(High) mode is observed at 437 cm^{-1}. In the E3 film, it is observed as a broader feature compared to E1 film. In the case of E5 film, the E_2(High) mode appears at 435 cm^{-1}. Lupan et al. also observed similar red shift in the E_2(High) frequency and broadening of E_2(High) mode with europium doping concentration. They suggested that the shift

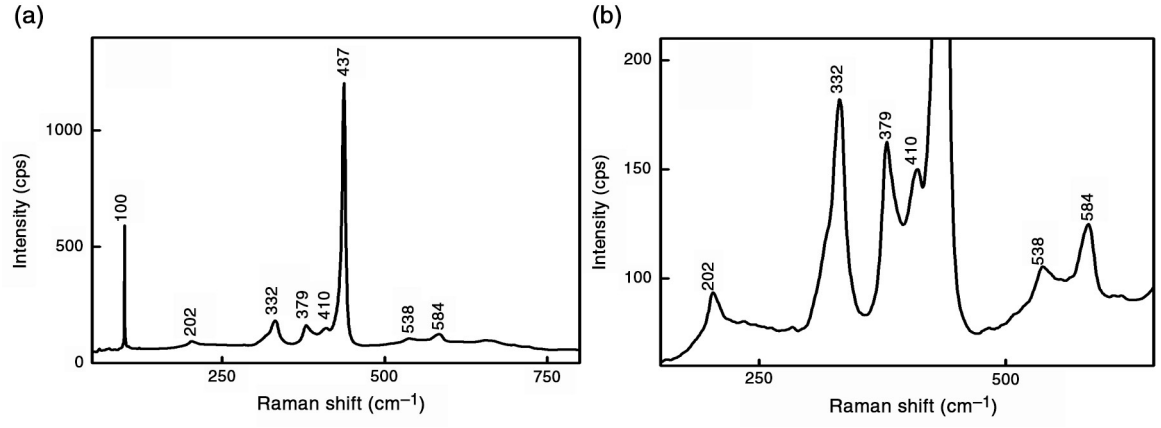

Fig. 2. Micro-Raman spectrum of (a) ZnO powder and (b) its enlarged spectrum showing weak bands.

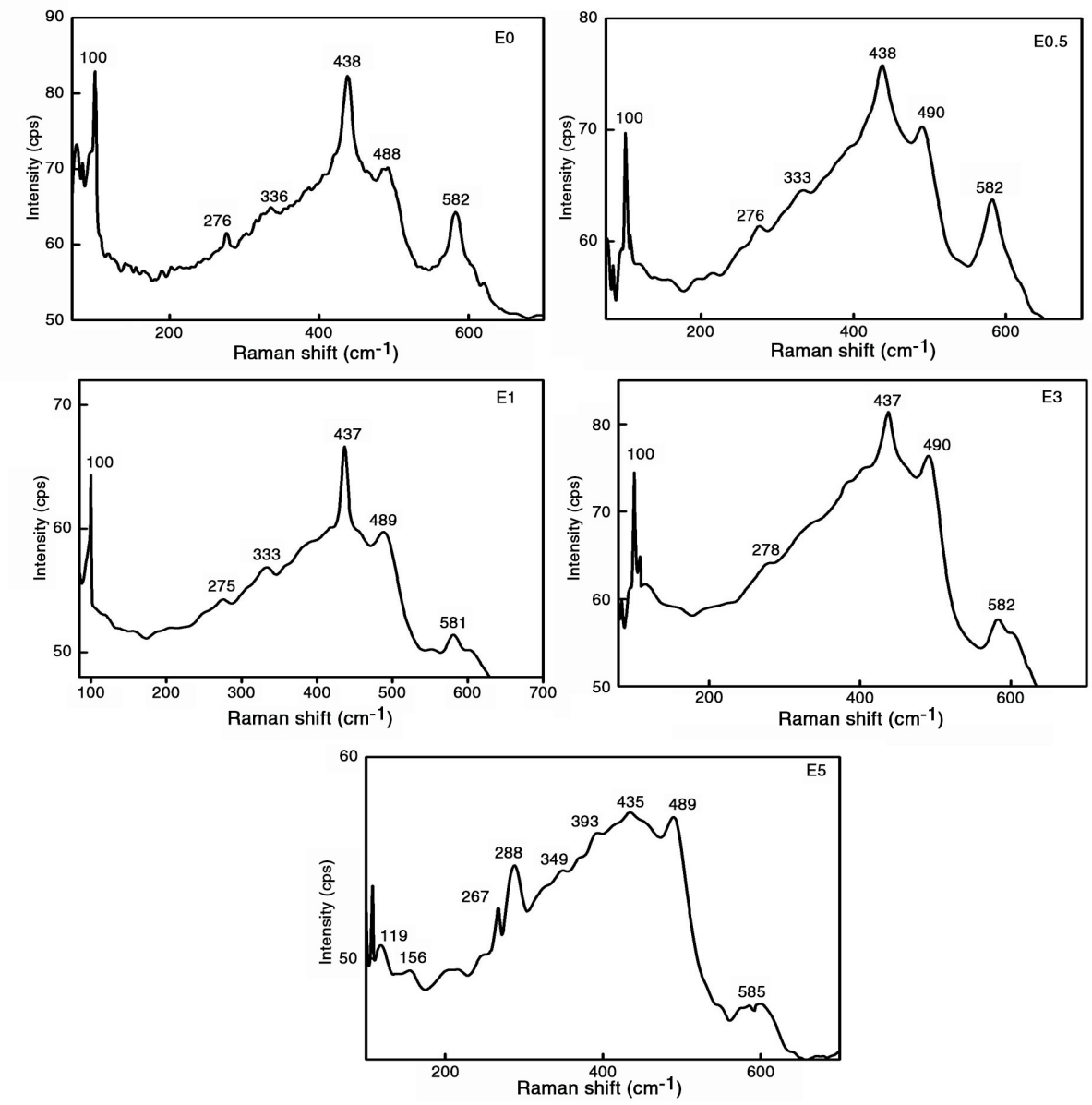

Fig. 3. Micro-Raman spectra of RF sputtered Eu_2O_3 doped ZnO films (Eu_2O_3 doping concentrations – 0, 0.5, 1, 3, and 5 wt%) on quartz substrates and annealed at 773K.

of E_2(High) mode towards lower wave numbers confirms the substitution of Zn^{2+} by Eu^{3+} ions in the ZnO lattice and the peak broadening indicates decline in crystalline quality of the films with europium doping (41, 42).

Bundesmann et al. reported an additional mode $\sim$275 cm^{-1} in doped ZnO films and they attributed it to intrinsic host lattice defects which become activated as vibrating complexes or their concentration increases up on dopant incorporation (43). Scepanovic et al. also reported an additional Raman band $\sim$275 and 284 cm^{-1} in ZnO which they attributed to intrinsic host lattice defects such as oxygen vacancies or zinc interstitials (44). In the Raman spectra of the pure (E0) and doped films (E0.5, E1 and E3), a less intense band is observed $\sim$276 cm^{-1} whereas in the E5 film two medium intense bands are observed $\sim$267 and 288 cm^{-1}. These bands are related to the defects in the films (45).

AFM analysis

Figure 4 shows the AFM images (3D) of undoped and Eu_2O_3 doped ZnO films. AFM image of undoped ZnO film presents uniform distribution of densely packed well-defined grains of more or less uniform size (around 45 nm) with well-defined grain boundaries. The surface

Citation: Nano Reviews 2015, **6**: 26759 - http://dx.doi.org/10.3402/nano.v6.26759

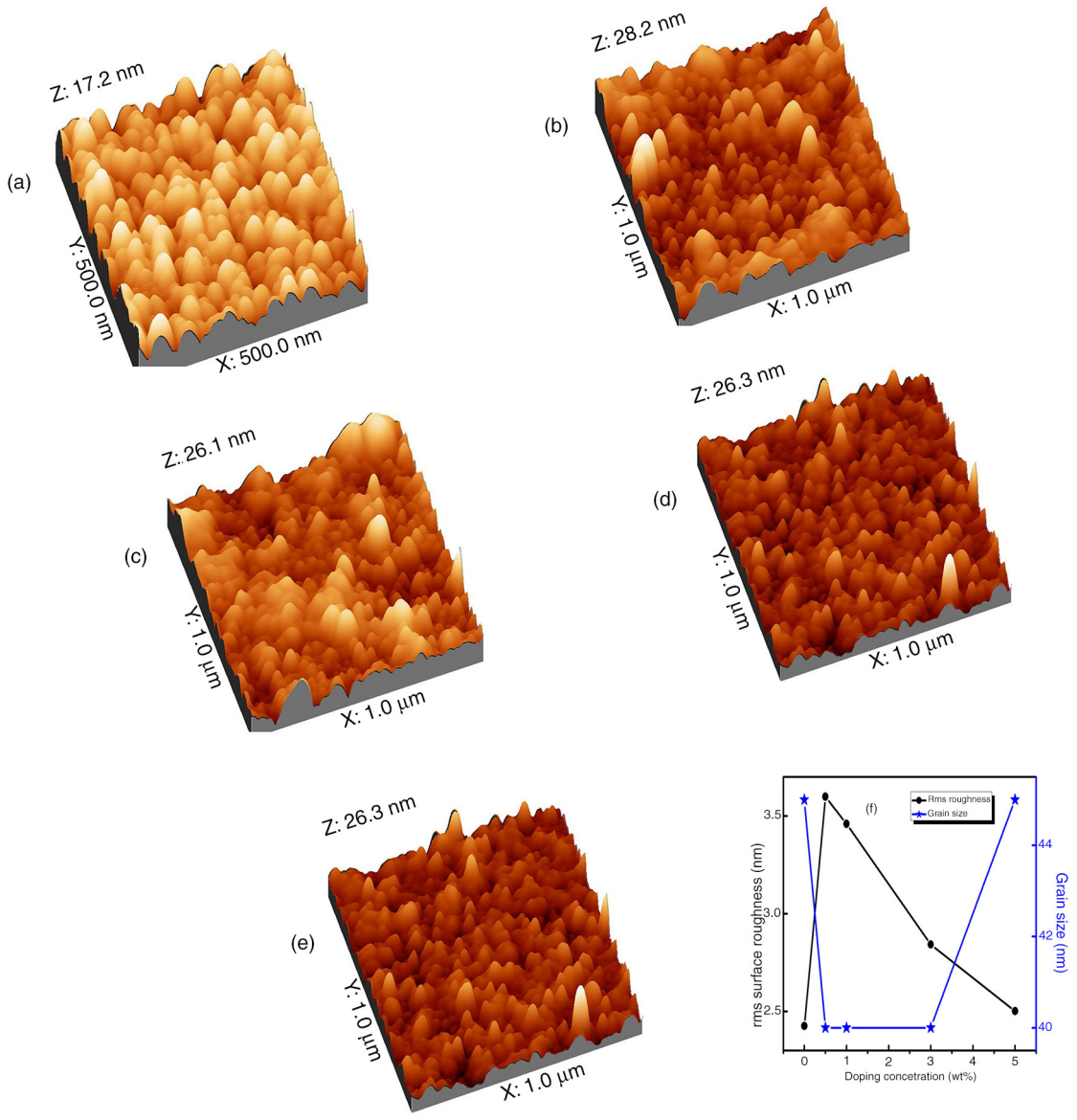

Fig. 4. 3D AFM micrographs of annealed ZnO films with different Eu_2O_3 doping concentrations (a) pure (b) 0.5 wt% (c) 1 wt% (d) 3 wt% (e) 5 wt%, and (f) variation of rms surface roughness and grain size with doping concentrations.

morphology of the Eu_2O_3 doped films presents dense distribution of grains. The E0.5 and E1 films show a tendency of coalescing smaller grains into bigger grains. The AFM images of E3 and E5 films show uniform dense distribution of smaller grains. The rms surface roughness of the films is estimated using WSXM4 software, as shown in Fig. 4(f) and Table 2. The films with Eu_2O_3 doping concentration 0.5 and 1wt% show higher rms surface roughness compared to the other films. The variation of the grain size with Eu_2O_3 doping concentration obtained from the AFM analysis (Table 2) shows the same trend as obtained from XRD analysis.

SEM and EDX analysis

SEM micrographs of Eu_2O_3 doped ZnO films are shown in Fig. 5. Similar to the AFM results, the SEM micrographs also present a smooth surface consisting of small grains of more or less equal size. The thickness measurements carried out using vertical SEM micrographs are shown in Fig. 6 and the thickness values are listed in Table 2.

Figure 7 shows the EDX spectra of the undoped and Eu_2O_3 doped ZnO films, annealed at 773K. The undoped ZnO film shows Zn and oxygen in equal ratio. The elemental analysis of the Eu_2O_3 doped ZnO films show the incorporation of Eu in the doped films.

Table 2. Morphological and optical parameters of RF sputtered pure and Eu_2O_3 doped ZnO films (Eu_2O_3 doping concentrations – 0, 0.5, 1, 3 and 5 wt%) on quartz substrates and annealed at 773K

	Thickness (nm) using					
Film	Stylus profilometer	Vertical SEM	RMS roughness (nm)	Transmittance (%)	Band gap (eV)	Refractive index at 550 nm
E0	83	89	2.4255	88	3.24	1.905
E0.5	82	96	3.5988	87	3.26	2.156
E1	82	96	3.4596	88	3.27	2.036
E3	87	117	2.8422	91	3.27	2.121
E5	94	116	2.5013	88	3.29	2.226

Optical properties

Figure 8 shows the transmittance and reflectance spectra of undoped and Eu_2O_3 doped ZnO films recorded in the wavelength range 200–900 nm. Average transmittance of the films in the wavelength range 400–900 nm are calculated and given in Table 2. All the films show very high

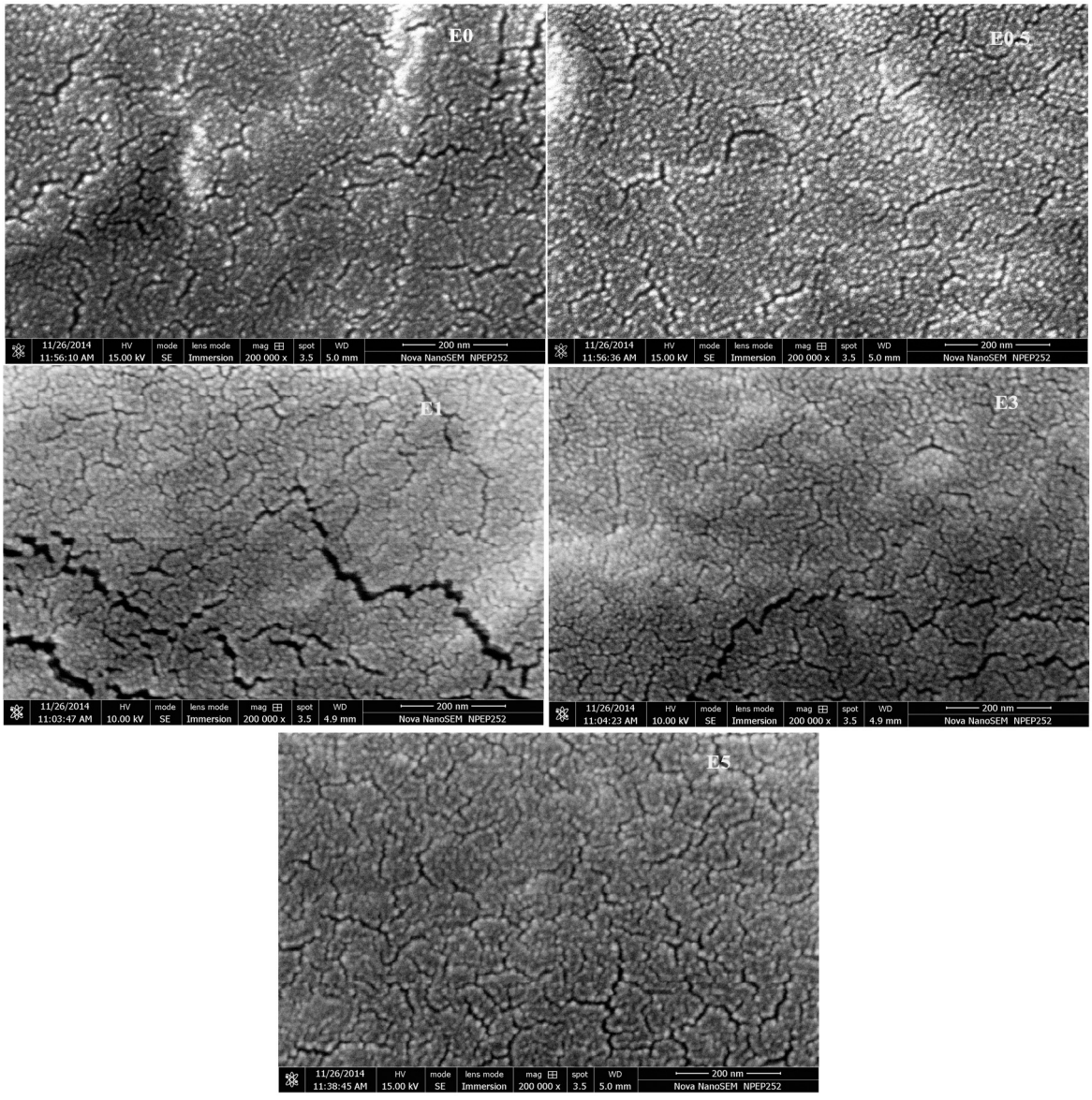

Fig. 5. SEM micrographs of RF sputtered Eu_2O_3 doped ZnO films (Eu_2O_3 doping concentrations – 0, 0.5, 1, 3, and 5 wt%) on quartz substrates annealed at a temperature of 773K showing the surface morphology.

Citation: Nano Reviews 2015, **6**: 26759 - http://dx.doi.org/10.3402/nano.v6.26759

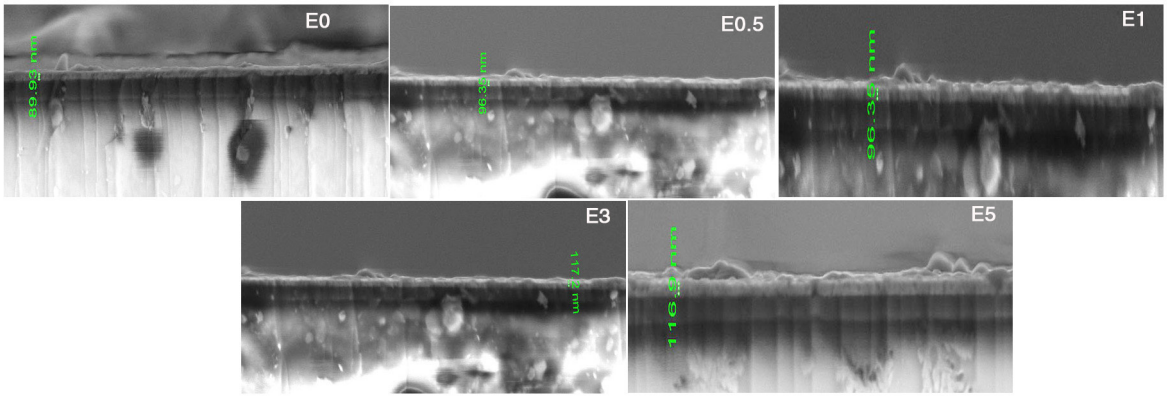

Fig. 6. The vertical SEM micrographs of RF sputtered Eu_2O_3 doped ZnO films (Eu_2O_3 doping concentrations – 0, 0.5, 1, 3, and 5 wt%) on quartz substrates annealed at 773K showing the thickness of the films.

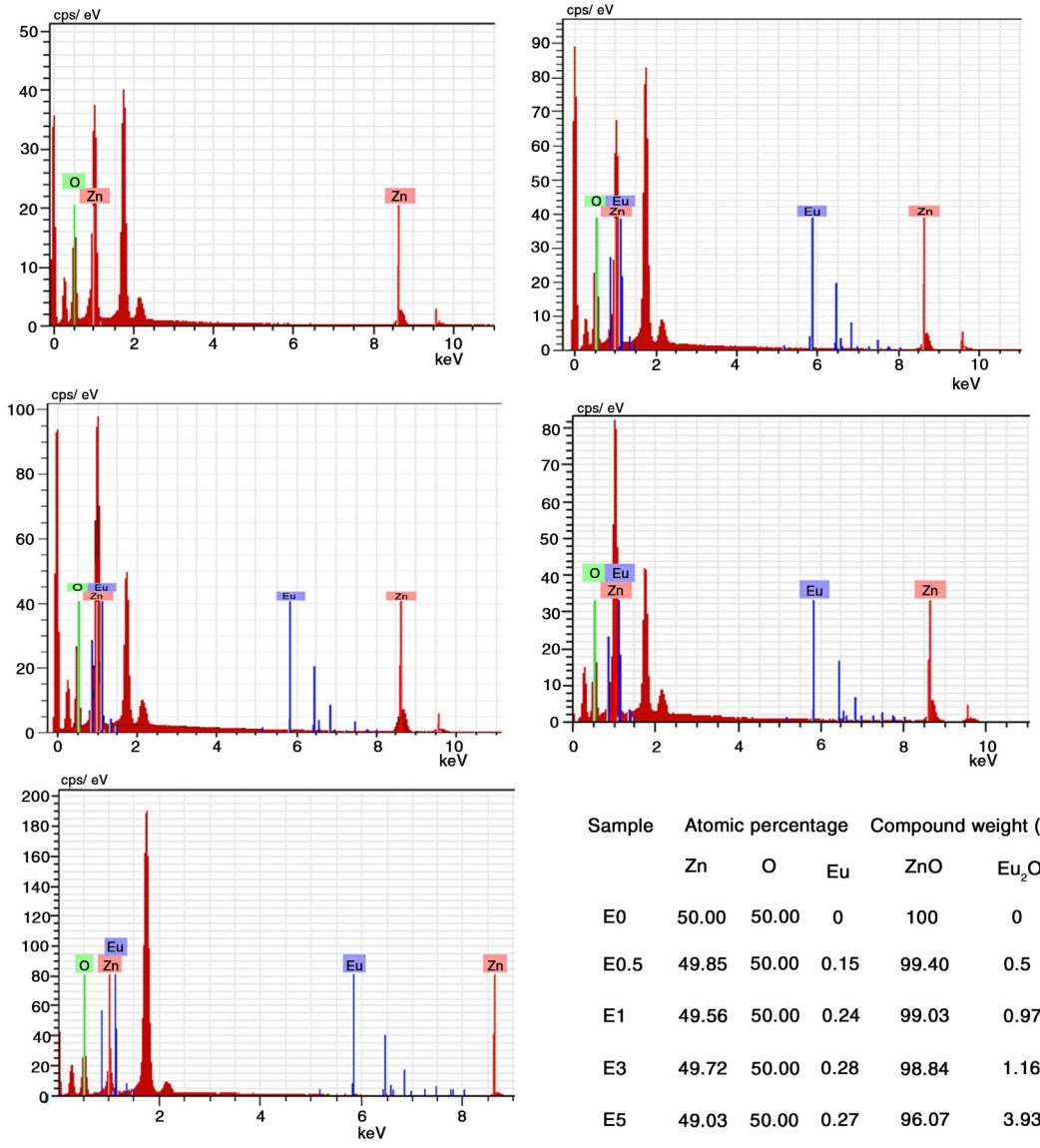

Sample	Atomic percentage			Compound weight (%)	
	Zn	O	Eu	ZnO	Eu_2O_3
E0	50.00	50.00	0	100	0
E0.5	49.85	50.00	0.15	99.40	0.5
E1	49.56	50.00	0.24	99.03	0.97
E3	49.72	50.00	0.28	98.84	1.16
E5	49.03	50.00	0.27	96.07	3.93

Fig. 7. The EDX spectra of RF sputtered Eu_2O_3 doped ZnO films (Eu_2O_3 doping concentrations – 0, 0.5, 1, 3, and 5 wt%) on quartz substrates annealed at 773K showing the elemental analysis.

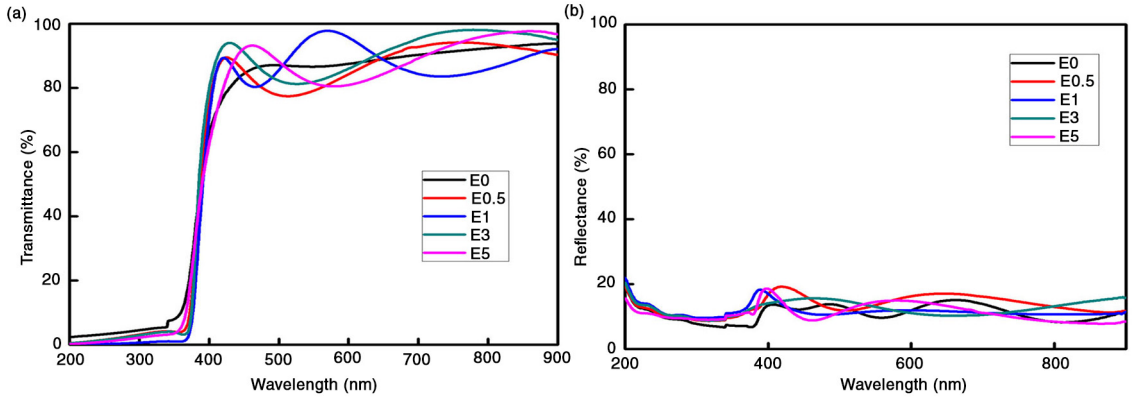

Fig. 8. UV-Visible spectra of undoped and Eu_2O_3 doped ZnO films (a) Transmittance spectra and (b) Reflectance spectra.

transmittance, above 87% in the visible region. For all the films the transmittance exhibits a sharp reduction at around 380 nm corresponding to the fundamental absorption edge of ZnO. The sharp absorption onset in the UV-region and high transmittance in the visible region indicates the good crystalline and optical quality and direct band gap nature of the films. The oscillations observed in the transmission and reflection spectra of the films can be due to the interference of light arising from the difference in refractive indices of the film and the substrate and the interference of multiple reflections arising from the film and substrate surface. These oscillations in the spectra indicate that smooth films are formed on quartz substrate as evident from the AFM analysis. Tan et al. also observed interference fringes in the transmittance spectra and suggested that the ZnO films had optically smooth surfaces and the interface with the quartz substrate is also smooth (46–49).

The optical absorption coefficient α can be calculated from the transmittance spectra using the following relation

$$\alpha = \frac{1}{t}\ln\left(\frac{1}{T}\right) \tag{8}$$

where t is the thickness of the film and T is the transmittance of the film. The optical band gap of the films are calculated using the relation (50),

$$\alpha h\nu = A(h\nu - E_g)^n \tag{9}$$

Where n can have values ½, $^3/_2$, 2 or 3 respectively for direct allowed, direct forbidden, indirect allowed and indirect forbidden transitions, h is the Plank's constant, ν is the frequency of the incident photon and A is the band edge constant depending on electron–hole mobility. The band gap E_g can be obtained by extrapolating the linear region of $(\alpha h\nu)^{1/n}$ vs. hν plot to $h\nu = 0$. The best fit for Tauc relation is observed for n=½ indicating direct allowed transition in these films. The Tauc plots of undoped and Eu_2O_3 doped ZnO films are shown in Fig. 9(a)–(e). Undoped film shows a band gap of 3.24 eV, which is smaller than the band gap of the bulk ZnO (3.37 eV) and Eu_2O_3 doped films show higher band gap values (Table 2). There are several reasons for the shift of band gap in the films such as improvement or reduction in crystallinity, modification in barrier height due to the change in crystallite dimension, quantum size effect, and change in the density of impurities, tensile or compressive strain in the films, and so on (51).

Huang et al. reported that a tensile strain produces a decrease in band gap whereas a compressive strain can result in an increase in band gap (52). XRD analysis shows that all the films exhibit compressive strain. Ziabari et al. suggested that the shift in band gap due to moderate or heavy doping is determined by two competing mechanisms: band gap narrowing which is a consequence of many body effects on the conduction and valance bands; and the band gap widening due to the well-known Burstein–Moss effect (53). The many body interaction effects leading to band gap narrowing may occur either between free carriers or between free carriers and ionized impurities (54, 55). According to quantum size effect, the band gap increases with decrease in particle size (56). It can be expected that the contribution from Eu^{3+} ions on substitutional sites of Zn^{2+} ions and Eu-interstitial atoms may determine the widening of the band gap caused by increase in carrier concentration. The Burstein–Moss effect explained the broadening of band gap energy with the increase in carrier concentration. Typically the blue shift of the absorption edge of the Eu_2O_3 doped ZnO films may be associated with an increase of the carrier concentration blocking the lowest states in the conduction band, which is well known as the Burstein-Moss effect (57).

Optical constants play an important role in design and fabrication of optical devices as they are closely related to the electronic polarizability of ions and the local field

Citation: Nano Reviews 2015, **6**: 26759 - http://dx.doi.org/10.3402/nano.v6.26759

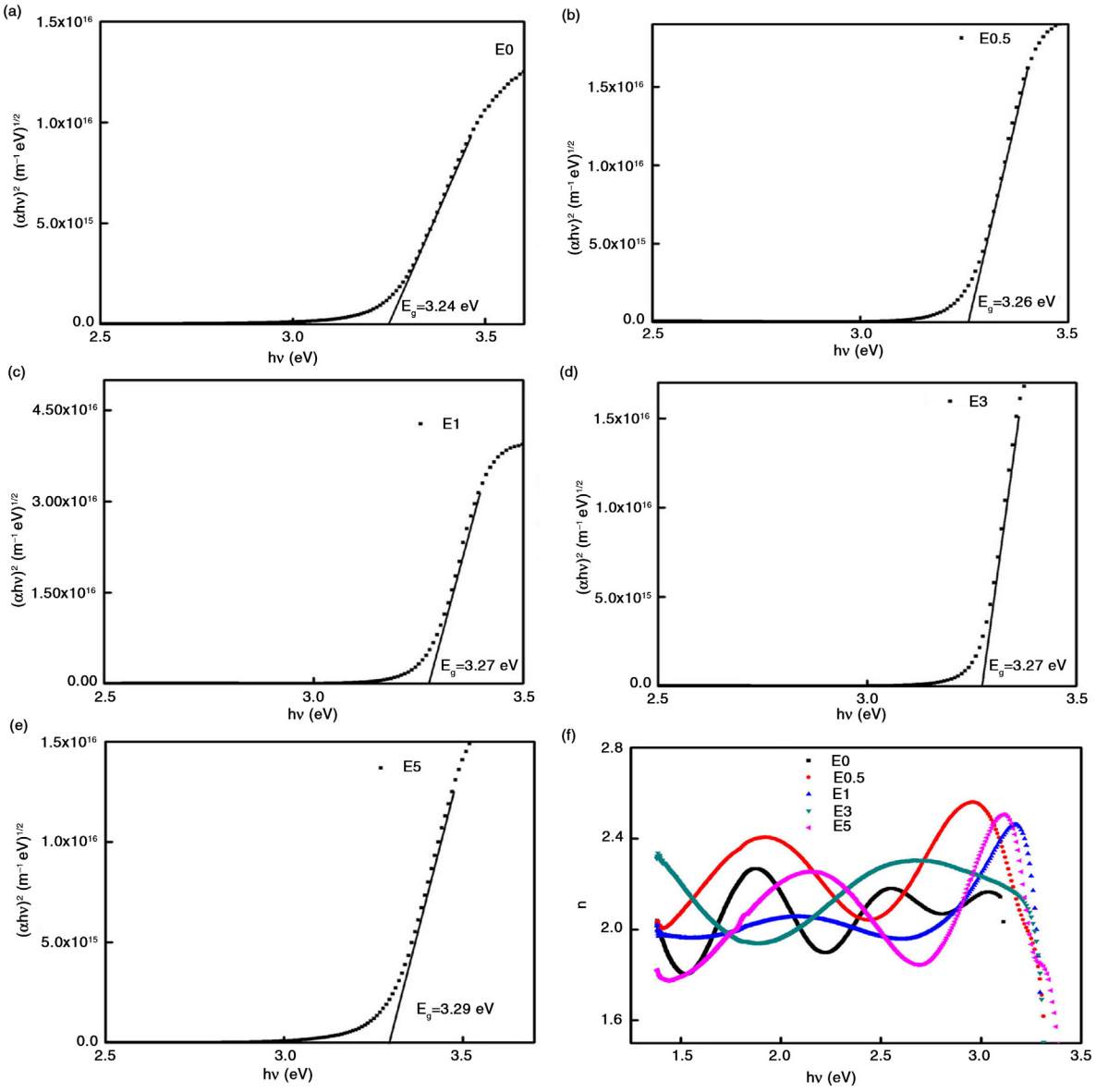

Fig. 9. Tauc plots of RF sputtered (a) pure and (b–e) Eu_2O_3 doped ZnO films (Eu_2O_3 doping concentrations – 0, 0.5, 1, 3 and 5 wt%) on quartz substrates and are annealed at a temperature 773K and (f) the variation of refractive indices of these films with photon energy.

inside the materials. The extinction coefficient k of the films is calculated using the equation

$$k = \frac{\alpha\lambda}{4\pi} \tag{10}$$

where α is the absorption coefficient and λ is the wavelength of incident light. The optical reflection from the film is directly related to the refractive index of the film by the following relation (58),

$$n = \frac{(1+R) + \sqrt{(1-R)^2 k^2}}{1-R} \tag{11}$$

where R is the reflectance of the film. The refractive indices of the films are found to be around 2, very close to the bulk value (Table 2). The E5 film shows the highest value of refractive index of 2.226 and the E0 film shows the lowest value of refractive index of 1.905. Figure 9(f) shows the variation of refractive index with incident photon energy.

The optical constants are closely related to the electronic polarizability of ions and the local field inside materials. Hence, the determination of optical constants plays a crucial role in the design of optical devices and optical communication systems (20, 59).

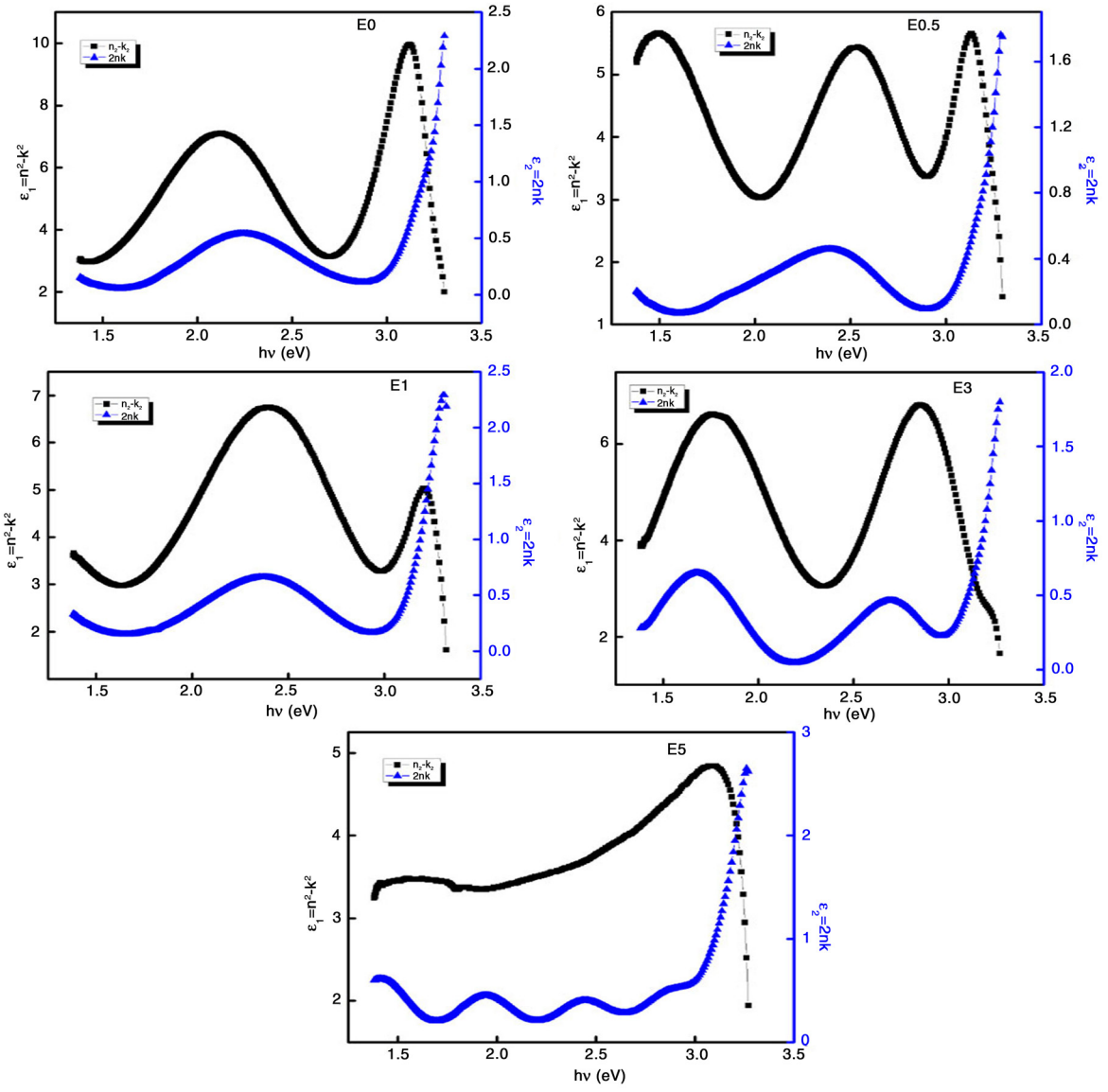

Fig. 10. Variation of real and imaginary parts of dielectric constants of undoped and Eu_2O_3 doped ZnO films as a function of photon energy.

The complex dielectric constant of the material can be defined as

$$\varepsilon(\lambda) = \varepsilon_r(\lambda) + i\varepsilon_i(\lambda) \tag{12}$$

The real and imaginary parts of the dielectric constant are related to n and k values by the relation

$$\varepsilon_r(\lambda) = n^2(\lambda) - k^2(\lambda) \tag{13}$$

and

$$\varepsilon_i(\lambda) = 2n(\lambda)k(\lambda). \tag{14}$$

The frequency dispersion of ε in the films can be obtained from the transmission and reflection spectra, which can provide the propagation, reflection, and loss of light in the films.

Figure 10 shows the dependence of real and imaginary parts of dielectric constant on wavelength, known as dispersion curve and absorption curve respectively. The values of real parts of dielectric constants are higher than that of imaginary parts. The real parts of dielectric constants of Eu_2O_3 doped ZnO films are found to be smaller than that of pure ZnO films. The variation of ε_r and refractive index follows similar trend, whereas the variation of ε_i follows the behavior of k. The variation of refractive index and extinction coefficients of the films as a function of photon energy is shown in Fig. 11.

The loss factor tand is the ratio of ε_i and ε_r (20). The variation of loss factor with wavelength of incident light is shown in Fig. 12. The loss factor is found to be increasing with Eu_2O_3 doping concentration.

Citation: Nano Reviews 2015, **6**: 26759 - http://dx.doi.org/10.3402/nano.v6.26759

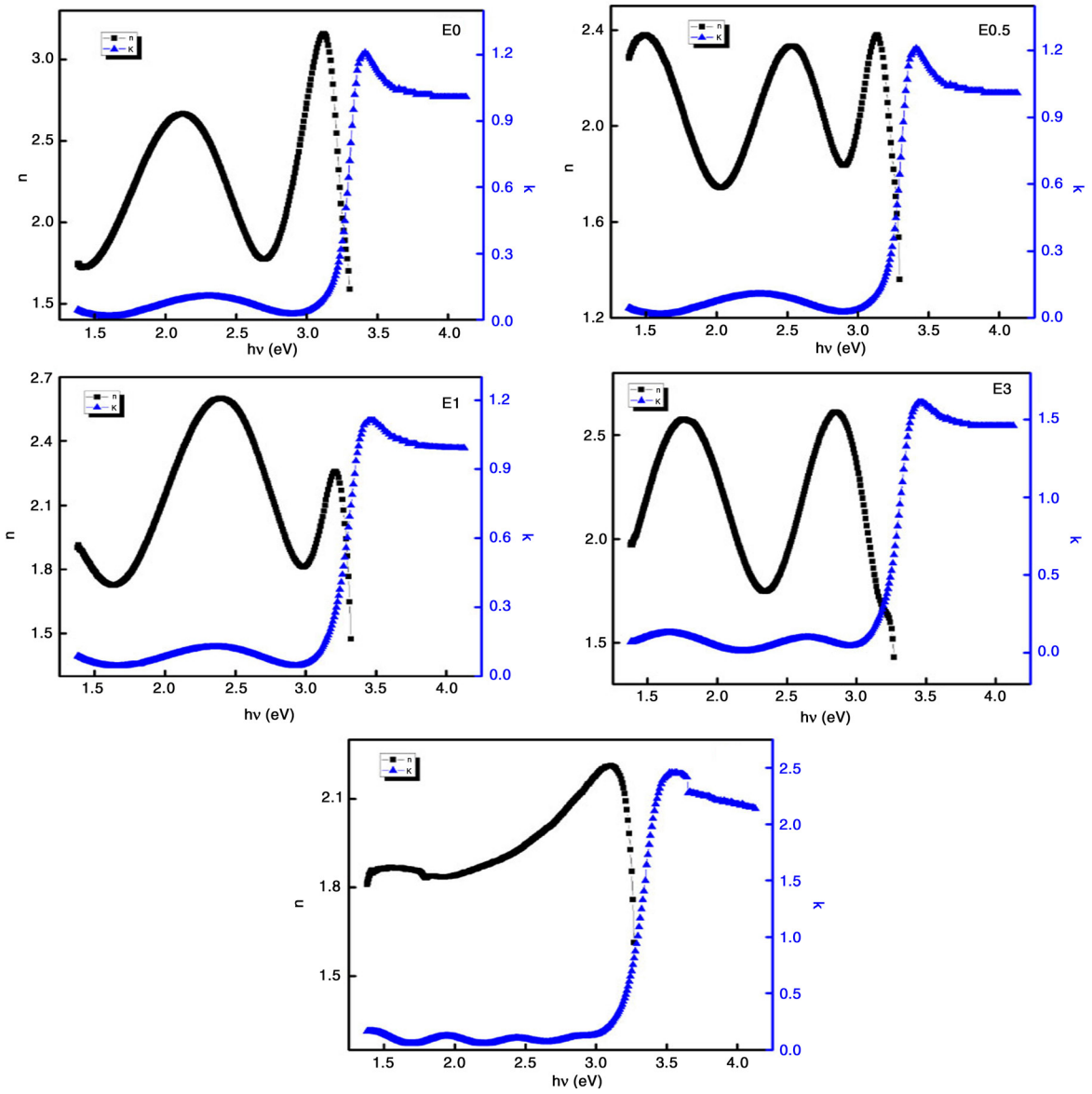

Fig. 11. Variation of refractive index and extinction coefficients of undoped and Eu_2O_3 doped ZnO films as a function of photon energy.

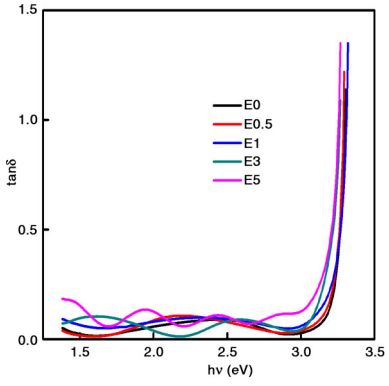

Fig. 12. Variation of loss factor of undoped and Eu_2O_3 doped ZnO films as a function of photon energy.

Photoluminescence spectra

Figure 13 shows the room temperature PL spectra of undoped and Eu_2O_3dopedZnO films recorded using excitation wavelength of 325 nm. The undoped film shows three main peaks at 409, 450, and 487 nm and a weak peak at 530 nm. The peak ~409 nm corresponds to near band edge emission (NBE) in ZnO which originates from the recombination of excitons. 0.5 wt% Eu_2O_3 doping has caused reduction in the peak intensity and broadening of the peaks. This effect continues with increase in doping concentration of Eu_2O_3. When the doping concentration of Eu_2O_3 was 5 wt%, these peaks are very weak.

The visible emissions observed may be due to the defects such as oxygen vacancy, Zn interstitials, antisite

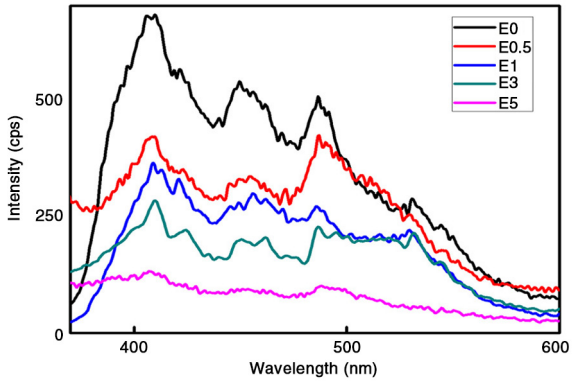

Fig. 13. Room temperature photoluminescence spectra of undoped and Eu_2O_3 doped ZnO films using excitation wavelength of 325 nm.

oxygen, and so on in the films. XRD and Raman results suggest the presence of tensile stress and formation of defects in the films. Zn interstitial (Zn_i) and oxygen vacancy (V_O) are the main donor defects while Zn vacancy (V_{Zn}) and oxygen interstitial (O_i) are the main acceptor defects in intrinsic ZnO (60). From the calculation using full-potential linear muffin-tin orbital (FP-LMTO) method by Sun the energy interval between the donor level of Zn interstitial and acceptor level of Zn vacancies is found to be ~2.6 eV (61–65). In the present case, the PL emission obtained ~487 nm corresponds to an energy 2.55 eV and hence it can be due to the transition between these levels. The green luminescence observed at 530 nm is generally attributed to intrinsic defects such as oxygen vacancies in the films (17).

Conclusion

Eu_2O_3 doped ZnO films are deposited on quartz substrate with various doping concentrations using RF magnetron sputtering. The structural, morphological, optical, and luminescent properties of the films are investigated. XRD analysis reveals the formation of nanostructured films exhibiting hexagonal wurtzite structure with (002) orientation. Micro-Raman spectra show high- and low-frequency E_2 modes indicating the hexagonal wurtzite structure of ZnO in the films. AFM image of undoped ZnO film presents uniform distribution of densely packed well-defined grains of more or less uniform size with well-defined grain boundaries. The surface morphology of the Eu_2O_3 doped films presents dense distribution of grains. All the films exhibit very good transparency in the visible region with a sharp cut-off around 380 nm. The appearance of interference fringes in the transmittance and reflectance spectra indicates good optical quality of the films. Band gap energy calculations using Tauc plot shows slight increase in the values of band gap with Eu_2O_3 doping. The photoluminescence spectra show both NBE and deep level emissions and the intensity of the peaks decreases with Eu_2O_3 doping concentration.

Conflict of interest and funding

There is no conflict of interest in the present study for any of the authors.

References

1. Klingshirn C. The luminescence of ZnO under high one- and two-quantum excitation. Phys Status Solidi B 1975; 71: 547–56.
2. Park S-M, Ikegami T, Ebihara K, Shin P-K. Structure and properties of transparent conductive doped ZnO films by pulsed laser deposition. Appl Surf Sci 2006; 253: 1522–7.
3. Nayak PK, Yang T, Kim J, Chung S, Jeong J, Lee C, et al. Spin-coated ZnO transparent conducting thin films for organic light-emitting diodes. J Phys Appl Phys 2009; 42: 035102. doi: 10.1088/0022-3727/42/3/035102.
4. Shan FK, Liu GX, Lee WJ, Shin BC. The role of oxygen vacancies in epitaxial-deposited ZnO thin films. J Appl Phys 2007; 101: 053106. doi: 10.1063/1.2437122.
5. Ohshima T, Thareja RK, Ikegami T, Ebihara K. Preparation of ZnO thin films on various substrates by pulsed laser deposition. Surf Coating Tech 2003; 169–70: 517–20.
6. Lupan O, Pauporte T, Chow L, Viana B, Pelle F, Ono LK, et al. Effects of annealing on properties of ZnO thin films prepared by electrochemical deposition in chloride medium. Appl Surf Sci 2010; 256: 1895–907.
7. Alim KA, Fonoberov VA, Shamsa M, Balandin AA. Micro-Raman investigation of optical phonons in ZnO nanocrystals. J Appl Phys 2005; 97: 124313. doi: 10.1063/1.1944222.
8. Lu JG, Fujita S, Kawaharamura T, Nishinaka H, Kamada Y. Junction properties of nitrogen-doped ZnO thin films. Phys Stat Sol C 2008; 5: 3088–90. doi: 10.1002/pssc.200779171.
9. Lee Y-C, Hu S-Y, Water W, Huang Y-S, Yang M-D, Shen J-L, et al. Improved optical and structural properties of ZnO thin films by rapid thermal annealing. Solid State Comm 2007; 143: 250–4.
10. Xu L, Shi L, Li X. Preparation of nanocone ZnO thin film and its aging effect of photoluminescence. Appl Surf Sci 2009; 255: 5957–60.
11. de Posada E, Tobin G, McGlynn E, Lunney JG. Pulsed laser deposition of ZnO and Mn-doped ZnO thin films. Appl Surf Sci 2003; 208–9: 589–93.
12. Heo YW, Ip K, Pearton SJ, Norton DP, Budai JD. Growth of ZnO thin films on c-plane Al_2O_3 by molecular beam epitaxy using ozone as an oxygen source. Appl Surf Sci 2006; 252: 7442–8.
13. Smirnov M, Baban C, Rusu GI. Structural and optical characteristics of spin-coated ZnO thin films. Appl Surf Sci 2010; 256: 2405–8.
14. Tan ST, Chen BJ, Sun XW, Fan WJ, Kwok HS, Zhang XH, et al. Blue shift of optical band gap in ZnO thin films grown by metal-organic chemical-vapor deposition. J Appl Phys 2005; 98: 013505. doi: 10.1063/1.1940137.
15. Lehraki N, Aida MS, Abed S, Attaf N, Attaf A, Poulain M. ZnO thin films deposition by spray pyrolysis: influence of precursor solution properties. Curr Appl Phys 2012; 12: 1283e1287. doi: 10.1016/j.cap.2012.03.012.
16. Bouderbala M, Hamzaoui S, Amrani B, Reshak AH, Adnane M, Sahraoui T, et al. Thickness dependence of structural, electrical and optical behaviour of undoped ZnO thin films. Physica B 2008; 403: 3326–30.
17. Vinodkumar R, Lethy KJ, Beena D, Detty AP, Navas I, Nayar UV, et al. Effect of ITO buffer layers on the structural, optical

Citation: Nano Reviews 2015, **6**: 26759 - http://dx.doi.org/10.3402/nano.v6.26759

and electrical properties of ZnO multilayer thin films prepared by pulsed laser deposition technique. Sol Energ Mater Sol Cell 2010; 94: 68–74.
18. Vinodkumar R, Lethy KJ, Beena D, Satyanarayana M, Jayasree RS, Ganesan V, et al. Effect of thermal annealing on the structural and optical properties of nanostructured zinc oxide thin films prepared by pulsed laser ablation. Sol Energ Mater Sol Cell 2009; 93: 74–8.
19. Vinodkumar R, Navas I, Chalana SR, Gopchandran KG, Ganesan V, Philip R, et al. Highly conductive and transparent laser ablated nanostructured Al: ZnO thin films. Appl Surf Sci 2010; 257: 708–16.
20. Vinodkumar R, Navas I, Porsezian K, Ganesan V, Unnikrishnan NV, Mahadevan Pillai VP. Structural, spectroscopic and electrical studies of nanostructured porous ZnO thin films prepared by pulsed laser deposition. Spectrochim Acta Mol Biomol Spectros 2014; 118: 724–32.
21. Deng H, Ressel JJ, Lamb RN, Jiang B, Li Y, Zhou XY. Microstructure control of ZnO thin films prepared by single source chemical vapor deposition. Thin Solid Films 2004; 458: 43–6. doi: 10.1016/j.tsf.2003.11.288.
22. Fujimura N, Nishihara T, Goto S, Xu J, Ito T. Control of preferred orientation for ZnO_x films: control of self texture. J Cryst Growth 1993; 130: 269–79.
23. Culity BD. Elements of X-ray diffraction. Reading, MA: Addison-Weseley; 1978, p. 102.
24. Mohantya P, Kima B, Park J. Synthesis of single crystalline europium-doped ZnO nanowires. Mater Sci Eng B 2007; 138: 224–7.
25. Guoqiang Q, Guanglei Z, Dongchun L, Shimin L. Lattice and internal relaxation of ZnO thin film under in-plane strain. Thin Solid Films 2010; 519: 378–84.
26. Puchert MK, Timbrell PY, Lamb RN. Post deposition annealing of radio frequency magnetron sputtered ZnO films. J Vac Sci Tech 1996; 14: 2220. doi: 10.1116/1.580050.
27. Illyaskutty N, Sreedhar S, Kohler H, Philip R, Rajan V, Mahadevan Pillai VP. ZnO-modified MoO3 nano-rods, -wires, -belts and -tubes: photophysical and nonlinear optical properties. J Phys Chem C 2013; 117; 7818–29. doi: 10.1021/jp311394y.
28. Li YF, Yao B, Lu YM, Cong CX, Zhang ZZ, Gai YQ, et al. Characterization of biaxial stress and its effect on optical properties of ZnO thin films. Appl Phys Lett 2007; 91: 021915.
29. Mohanty BC, Jo YH, Yeon DH, Choi IJ, Cho YS. Stress-induced anomalous shift of optical band gap in ZnO: Al thin films. Appl Phys Lett 2009; 95: 062103. doi: 10.1063/1.3202399.
30. Srikant V, Clarke DR. Optical absorption edge of ZnO thin films: the effect of substrate. J Appl Phys 1997; 81: 6357–64. doi: 10.1116/1.580050.
31. Malek MF, Mamat MH, Khusaimi Z, Sahdan MZ, Musa MZ, Zainun AR, et al. Sonicated sol–gel preparation of nanoparticulate ZnO thin films with various deposition speeds: the highly preferred c-axis (002) orientation enhances the final properties. J Alloy Comp 2014; 582: 12–21.
32. Fateley WG, Dollish FR, Mc Devitt NT, Bentley FF. Infrared and Raman selection rules for molecular and Lattice vibrations – the correlation method. New York: Wiley-Interscience; 1972.
33. Zeferino RS, Flores MB, Pal U. Photoluminescence and Raman scattering in Ag-doped ZnO nanoparticles. J Appl Phys 2011; 109: 014308. doi: 10.1063/1.3530631.
34. Alim KA, Fonoberov VA, Shamsa M, Balandin AA. Micro-Raman investigation of optical phonons in ZnO nanocrystals. J Appl Phys 2005; 97: 124313.
35. Salman KA, Omar K, Hassan Z. Effective conversion efficiency enhancement of solar cell using ZnO/PS antireflection coating. Sol Energ 2012; 86: 541–7.
36. Koyano M, Quocbao P, Thanbbinh LT, Hongha L, Ngoclong N, Katayama S. Photoluminescence and Raman spectra of ZnO thin films by charged liquid cluster beam technique. Phys Status Solidi 2002; 193: 125–31.
37. Chen SJ, Liu YC, Lu YM, Zhang JY, Shen DZ, Fan XW. Photoluminescence and Raman behavior of ZnO nanostructures with different morphologies. J Cryst Growth 2006; 289: 55–8.
38. Zhaochun Z, Baibiao H, Yongqin Y, Deliang C. Electrical properties and Raman spectra of undoped and Al-doped ZnO thin films by metalorganic vapor phase epitaxy. Mater Sci Eng B 2001; 86: 109–12.
39. Zhang B, Zhang X-T, Gong H-C, Wu Z-S, Zhou S-M, Du Z-L. Ni-doped zinc oxide nanocombs and phonon spectra properties. Phys Lett 2008; 372: 2300–3.
40. Zhang T, Zeng Y, Fan HT, Wang LJ, Wang R, Fu WY, et al. Synthesis, optical and gas sensitive properties of large-scale aggregative flowerlike ZnO nanostructures via simple route hydrothermal process. J Phys Appl Phys 2009; 42: 045103. doi: 10.1088/0022-3727/42/4/045103.
41. Lupan O, Pauporte T, Viana B, Aschehoug P, Ahmadi M, Cuenya BR, et al. Eu-doped ZnO nanowire arrays grown by electrodeposition. Appl Surf Sci 2013; 282: 782–8.
42. Huang Y, Liu M, Li Z, Zeng Y, Liu S. Raman spectroscopy study of ZnO-based ceramic films fabricated by novel sol-gel process. Mater Sci Eng B 2003; 97: 111–16.
43. Bundesmann C, Ashkenov N, Schubert M, Spemann D, Butz T, Kaidashev EM, et al. Raman scattering in ZnO thin films doped with Fe, Sb, Al, Ga, and Li. Appl Phys Lett 2003; 83: 1974. doi: 10.1063/1.1609251.
44. Scepanovic M, Srećkovic T, Vojisavljevic K, Ristic MM. Modification of the structural and optical properties of commercial ZnO powder by mechanical activation. Sci Sinter 2006; 38: 169–75. doi: 10.2298/SOS0602169S.
45. Du CL, Gu ZB, Lu MH, Wang J, Zhang ST, Zhao J, et al. Raman spectroscopy of (Mn, Co)-codoped ZnO films. J Appl Phys 2006; 99: 123515. doi: 10.1063/1.2208298.
46. Swanepoel R. Determination of surface roughness and optical constants of inhomogeneous amorphous silicon films. J Phys E Sci Instrum 1983; 16: 12–14.
47. Lethy KJ, Pandya S, Beena D, Vinodkumar R, Sathe V, Mahadevan Pillai VP. Transparent and low resistive nanostructured laser ablated tungsten oxide thin films by nitrogen doping: II.Substrate temperature. J Phys D Appl Phys 2009; 42: 185407. doi: 10.1088/0022-3727/42/18/185407.
48. Bose RJ, Kumar RV, Sudheer SK, Reddy VR, Ganesan V, Mahadevan Pillai VP. Effect of silver incorporation in phase formation and band gap tuning of tungsten oxide thin films. J Appl Phys 2012; 112: 114311. doi: 10.1063/1.4768206.
49. Tan ST, Chen BJ, Sun XW, Fan WJ, Kwok HS, Zhang XH, et al. Blue shift of optical band gap in ZnO thin films grown by metal-organic chemical-vapor deposition. J Appl Phys 2005; 98: 013505. doi: 10.1063/1.1940137.
50. Tauc J. Optical properties of amorphous semiconductors. Amorphous and liquid semiconductors. London: Plenum; 1974.
51. Suchea M, Christoulakis S, Kartharakis M, Vidakis N, Koudoumas E. Influence of thickness and growth temperature on the optical and electrical properties of ZnO thin films. Thin Solid Films 2009; 517: 4303–6.
52. Huang H, Ou Y, Xu S, Fang G, Li M, Zhao XZ. Properties of Dy-doped ZnO nanocrystalline thin films prepared by pulsed laser deposition. Appl Surf Sci 2008; 254: 2013–16.
53. Ziabari AA, Rozati SM. Carrier transport and bandgap shift in n-type degenerate ZnO thinfilms: the effect of bandedge nonparabolicity. Physica B 2012; 407: 4512–17.

54. Kim CE, Moon P, Kim S, Myoung J-M, Jang HW, Bang J, et al. Effect of carrier concentration on optical bandgap shift in ZnO:Ga thin films. Thin Solid Films 2010; 518: 6304–7.
55. Lethy KJ, Beena D, Mahadevan Pillai VP, Ganesan V. Bandgap renormalization in titania modified nanostructured tungsten oxide thin films prepared by pulsed laser deposition technique for solar cell applications. J Appl Phys 2008; 104: 033515.
56. Sreeja R, John J, Aneesh PM, Jayaraj MK. Linear and non-linear optical properties of luminescent ZnO nanoparticles embedded in PMMA matrix. Optic Comm 2010; 283: 2908–13.
57. Burstein E. Anomalous optical absorption limit in InSb. Phys Rev 1954; 93: 632.
58. Chen Y, Bagnall DM, Koh HJ, Park KT, Hiraga K, Zhu ZQ, et al. Plasma assisted molecular beam epitaxy of ZnO on *c*-plane sapphire: growth and characterization. J Appl Phys 1998; 84: 3912–18. doi: 10.1063/1.368595.
59. Khan MAM, Khan MW, Alhoshan M, AlSalhi MS, Aldwayyan AS. Influences of Co doping on the structural and optical properties of ZnO nanostructured. Appl Phys A 2010; 100: 45–51. doi: 10.1007/s00339-010-5840-8.
60. Peng X, Xu J, Zang H, Wang B, Wang Z. Structural and Pl properties of Cu doped ZnO films. J Lumin 2008; 128: 297–300.
61. Lin B, Fu Z, Jia Y. Green luminescent center in undoped zinc oxide films deposited on silicon substrates. Appl Phys Lett 2001; 79: 943.
62. Vanhensden K, Seager CH, Warren WL, Tallant DR, Voigt JA. Correlation between photoluminescence and oxygen vacancies in ZnO phosphors. Appl Phys Lett 1996; 68: 403. doi: 10.1063/1.116699.
63. Wei XQ, Man BY, Liu M, Xue CS, Zhuang HZ, Yang C. Blue luminescent centers and microstructural evaluation by XPS and Raman in ZnO thin films annealed in vacuum, N_2 and O_2. Physica B 2007; 388: 145–52.
64. Sun YM. PhD. Thesis, University of Science and Technology of China, July 2000.
65. Cao B, Cai W, Zeng H, Duan G. Morphology evolution and photoluminescence properties of ZnO films electrochemically deposited on conductive glass substrates. J Appl Phys 2006; 99: 073516. doi: 10.1063/1.2188132.

***V. P. Mahadevan Pillai**
Department of Optoelectronics
University of Kerala
Kariavattom, Thiruvananthapuram
Kerala 695581
India
Email: vpmpillai9@gmail.com

Citation: Nano Reviews 2015, **6**: 26759 - http://dx.doi.org/10.3402/nano.v6.26759